

Strong lensing of light and shadow of a Black Hole surrounded by a heavy accretion disk

Nelson António Eiró da Silva, 90996¹

¹*Departamento de Física, Instituto Superior Técnico - IST,
Universidade de Lisboa - UL, Avenida Rovisco Pais 1, 1049-001, Portugal*

(Dated: October 2019)

In this work, we study the superposition of a Schwarzschild Black Hole and a thin but massive disk composed of counterrotating particles [1]. The analysis of this solution shows that, for a certain set of parameters, namely the central Black Hole mass M_{BH} , and the inner edge of the disk a , the solution is astrophysically relevant, in contrast to other solutions [2], which have tachyonic velocities. Moreover, because the disk is massive, and not just a massless test disk, it deforms the spacetime. We can study the deformation caused by the system Black Hole + Disk by comparison with the Schwarzschild Black Hole solution. To do so, we numerically integrate null geodesics with a Runge-Kutta-Fehlberg algorithm with adaptive step the Shadow and the Lensing of both systems, using the backwards ray-tracing technique.

1. INTRODUCTION

Not long had passed since the formulation of General Relativity by Albert Einstein in 1915, when Karl Schwarzschild, in 1916, discovered the first exact solution of the vacuum Einstein's field equations. This solution was [3] spherically symmetric, static and asymptotically flat. Moreover, by Birkhoff's theorem [4], Schwarzschild's solution is the most general spherically symmetric solution to the vacuum field equations, as well as the simplest Black Hole solution known, without charge or angular momentum. The metric that describes the Schwarzschild solution is given in Schwarzschild coordinates by [3]

$$ds^2 = - \left(1 - \frac{2M}{r} \right) dt^2 + \frac{1}{1 - \frac{2M}{r}} dr^2 + r^2 d\theta^2 + r^2 \sin^2 \theta d\varphi^2, \quad (1)$$

where M is the mass of the Black Hole, being the only parameter that characterizes it. Other Black Hole have been found, such as rotating and/or charged Black Holes.

However, it is known by uniqueness theorems (see *e.g.* [5, 6] for a review) that the Kerr Black Hole (Black Hole with angular momentum J), alongside with the Kerr-Newman Black Hole (Black Hole that has both charge Q and angular momentum J), are "the only stationary, asymptotically flat solutions of the source free Einstein-Maxwell equations with no naked singularities". Despite these theorems, there is still no experimental confirmation that astrophysical black holes are described by the Kerr metric.

Amongst the observables that can be used to test the true nature of the spacetime around astrophysical Black Holes, we find their shadow: the representation of the light that comes from the event horizon of a Black Hole (the boundary that encloses a region in spacetime where due to the causal structure, prevents anything to escape from it, even light), that due to its characteristics is in fact the absence of electromagnetic radiation [7].

This is precisely what the Event Horizon Telescope (EHT) has tried to observe. The EHT is a very long

baseline interferometry array of telescopes that work in the millimeter and submillimeter wavelength, placed around the globe [8].

The EHT collaboration has two main targets: the Supermassive Black Hole at the center of the galaxy M87, and Sgr A* at the center of Milky Way. For one of the targets, the Supermassive Black Hole at the center of the galaxy M87, data was acquired in 2017, and results were presented in 2019 [8–13]: for the first time, we could see the shadow of a Black Hole (figure 1). These results open doors for us to test broad aspects of Black Holes' phenomenology [14, 15].

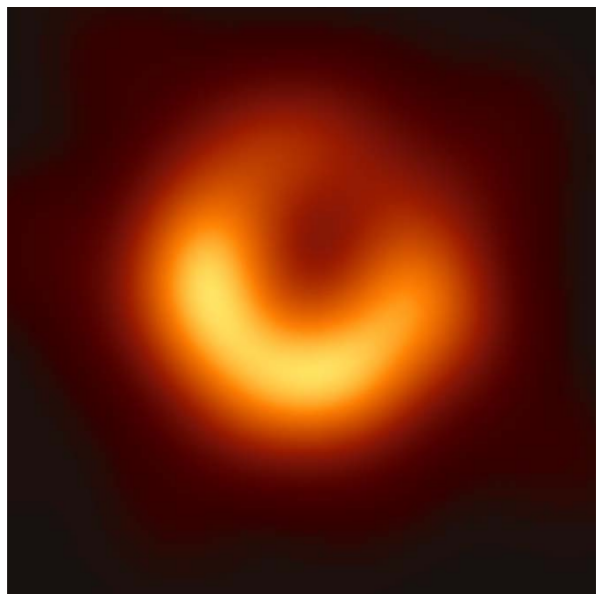


FIG. 1: The image of the Shadow of the Supermassive Black Hole at the center of M87. Adapted from [11].

2. WEYL SOLUTIONS AND THE ACCRETION DISK

Due to the spherical symmetry of the Schwarzschild Black Hole solution, its spacetime is usually studied in Schwarzschild coordinates. However, when we talk about a disk that is axisymmetric (and in this case, will be superposed to the Black Hole), the disk solution is more naturally written in (cylindrical) Weyl's canonical coordinates (t, ρ, z, φ) , that has a general metric given by

$$ds^2 = -e^{\phi(\rho,z)} dt^2 + e^{\nu(\rho,z) - \phi(\rho,z)} (d\rho^2 + dz^2) + \rho^2 e^{-\phi(\rho,z)} d\varphi^2, \quad (2)$$

where $\nu(\rho, z)$ and $\phi(\rho, z)$ are metric functions, that will be interpreted as gravitational potentials.

We have then to choose which coordinates simplify the process of studying the Black Hole + disk solution. In fact, by solving Einstein's equations in vacuum ($T_{\mu\nu} = 0$) for the metric given in equation 2, we verify that the potential ϕ satisfies the Laplace equation in 3-dimensional cylindrical coordinates

$$\phi_{,\rho\rho} + \frac{\phi_{,\rho}}{\rho} + \phi_{,zz} = 0. \quad (3)$$

That is, one of the Einstein's equations is linear, and so the superposed solution of the Black Hole + disk is the sum of the two solutions (due to the linearity of Laplace's equation).

The other equation to compute $\nu[\phi]$ is found by integration from the point (ρ, z) to infinity (throughout the text, the notation for the derivative of a quantity, say A , with respect to a coordinate (for example z) is written with a subscript comma as $A_{,z}$).

$$\nu[\phi] = \frac{1}{2} \int \rho [(\phi_{,\rho}^2 - \phi_{,z}^2) d\rho + 2\phi_{,\rho}\phi_{,z} dz]. \quad (4)$$

2.1. Schwarzschild Black Hole in Weyl coordinates

A priori, we do not know the potentials Ψ and $\nu[\Psi]$ for the Schwarzschild Black Hole in Weyl coordinates. But when we change coordinates from (t, r, θ, φ) in equation 1 to (t, ρ, z, φ) in equation 2, the corresponding metric elements must be geometrically equivalent. With the help of [16], we have the relations between Schwarzschild and Weyl coordinates

$$\rho = \sqrt{r(r-2M)} \sin \theta, \quad (5a)$$

$$z = (r-M) \cos \theta. \quad (5b)$$

By a simple differentiation ($d(\rho, z) = \frac{\partial(\rho,z)}{\partial r} dr + \frac{\partial(\rho,z)}{\partial \theta} d\theta$), we have the expressions for $d\rho$ and dz that we can plug into equation 2 to have

$$ds^2 = -e^{\Psi} dt^2 + e^{\nu-\Psi} \left[\frac{\Sigma}{r^2(1-2M/r)} dr^2 + \Sigma d\theta^2 \right] + r^2 \left(1 - \frac{2M}{r} \right) \sin^2 \theta e^{-\Psi} d\varphi^2, \quad (6)$$

where $\Sigma = (r-M)^2 - M^2 \cos^2 \theta$. Comparison with equation 1 gives us the final form of the metric potentials

$$\Psi = \log \left(1 - \frac{2M}{r} \right), \quad (7a)$$

$$\nu[\Psi] = \log \left(\frac{r(r-2M)}{\Sigma} \right). \quad (7b)$$

With the help of [16] we introduce the quantities d_1 and d_2 defined as $d_{1,2} = \sqrt{\rho^2 + (z \mp M)^2}$ and by inverting the first equation of 5 as $r = M + \frac{1}{2}(d_1 + d_2)$, we can rewrite the potentials in equation 7 in cylindrical coordinates as

$$\Psi = \log \left(\frac{d_1 + d_2 - 2M}{d_1 + d_2 + 2M} \right), \quad (8a)$$

$$\nu[\Psi] = \log \left(\frac{(d_1 + d_2)^2 - 4M^2}{4\Sigma} \right). \quad (8b)$$

Equation 8a can be identified ([17]) as the Newtonian potential of an infinitely thin rod, located in the axis $\rho = 0$ and with $|z| \leq M$. Moreover, we can see from equation 5 that $r = 2M$ (the Schwarzschild radius) corresponds to $\rho = 0$ and $z = M \cos \theta$, that is, the Schwarzschild Black Hole is described by a line segment in $\rho = 0$ with $-M \leq z \leq M$, being M the mass of the Black Hole. In this line segment, we have that the potential $\Psi = -\infty$.

2.2. Thin disk solution

One might naturally think that disks around Black Holes are (almost) massless (so-called test disks), consequently not being important to the geometry of the spacetime around the system. However, we can consider a more interesting and astrophysically relevant case: a thin but massive disk placed around a Black Hole, that can have a significant effect in the structure of spacetime.

Prior to Lemos and Letelier study, one other static axially symmetric disk solution, which possesses an outer edge, but not an inner edge, was already known by Morgan and Morgan [2]. However, Morgan-Morgan disks

are not astrophysically satisfactory: some of the particles that compose the disk possess tachyonic speeds up to the edge of the disk [1].

The solution found by Lemos and Letelier is a more astrophysically relevant one: by inverting the Morgan-Morgan disk, Lemos and Letelier constructed a static solution of a disk with an inner edge, made of counter-rotating particles [18], with "as many particles rotating to one side as to the other" [1]. The result of this counterrotation is a zero net angular momentum, and consequently a static disk with a centrifugal balance when a central Black Hole is present.

We start from the expression for the Morgan-Morgan disk potential Λ that is expressed as ([2])

$$\Lambda = -\frac{2M}{a} \left\{ \cot^{-1} \xi + \frac{1}{4} [(3\xi^2 + 1) \cot^{-1} \xi - 3\xi] \times (3\eta^2 - 1) \right\}, \quad (9)$$

where $\rho = a$ is the location of the outer edge of the disk and M is the mass of the disk; and where (ξ, η) are oblate ellipsoidal coordinates. These are connected to Weyl coordinates by

$$\rho^2 = a^2(1 + \xi^2)(1 - \eta^2), \quad (10a)$$

$$z = a\xi\eta, \quad (10b)$$

with $-1 \leq \eta \leq 1$ and $0 \leq \xi < \infty$. We proceed by inverting equations 10 in order to write ξ and η in terms of ρ and z . As pointed out previously, Morgan-Morgan disks have an outer edge, but not an inner edge. The process to obtain a disk with an inner edge is accomplished by performing a sort of inversion called a Kelvin transformation [19] on the coordinates (ρ, z) as

$$(\rho, z) \rightarrow \frac{a^2}{\rho^2 + z^2}(\rho, z), \quad (11)$$

where $\rho = a$ is now the inner edge of the (Lemos-Letelier) disk. Carrying out with this process, we reach at the formula for the inverted Morgan-Morgan (or Lemos-Letelier) massive disk, with mass \bar{M} and inner edge a , given explicitly by

$$\bar{\Lambda} = \frac{\bar{M} \sqrt{a^2 + \sqrt{a^4 + 2a^2(z^2 - \rho^2) + (\rho^2 + z^2)^2} - \rho^2 - z^2} \left(-3a^2 + 3\sqrt{a^4 + 2a^2(z^2 - \rho^2) + (\rho^2 + z^2)^2} + \rho^2 + z^2 \right)}{\sqrt{2}\pi(\rho^2 + z^2)^2} - \frac{2\bar{M} \left(a^2(2z^2 - \rho^2) + 2(\rho^2 + z^2)^2 \right) \tan^{-1} \left(\sqrt{2} \sqrt{\frac{\rho^2 + z^2}{a^2 + \sqrt{a^4 + 2a^2(z^2 - \rho^2) + (\rho^2 + z^2)^2} - \rho^2 - z^2}} \right)}{\pi(\rho^2 + z^2)^{5/2}}, \quad (12)$$

where the relation $\cot^{-1}(\xi) = \tan^{-1}(1/\xi)$ ($\xi > 0$) was used. The masses M and \bar{M} identified in the equation of the disks 9, 12 are also different: the Newtonian density of the Morgan-Morgan disk is given by [20, 21]

$$S = \frac{3M}{2\pi a^3} (a^2 - \rho^2) \delta(z) \quad , \rho \leq a. \quad (13)$$

and the relationship with the Newtonian density \bar{S} of the Lemos-Letelier disk is given by

$$\bar{S}(\rho) = \left(\frac{a}{\rho} \right)^3 S \left(\frac{a^2}{\rho} \right) \delta(z). \quad (14)$$

Integrating equation 14 as $\iiint \bar{S}(\rho, z) \rho d\rho dz d\varphi$ yields the result $\frac{3}{4}\pi\bar{M}$. However, the integration of the Newtonian density \bar{S} in cylindrical 3-space (ρ, z, φ) must be equal to the mass of the Lemos-Letelier disk \bar{M} , and so the relation between the two is $\bar{M} = \frac{3M\pi}{4}$.

2.3. The behavior of $\bar{\Lambda}$

The Lemos-Letelier disk potential (equation 12) is placed at $z = 0$ (acting like a Dirac-delta at $z = 0$: $\delta(z)$), is continuous everywhere. However, at $z = 0$ the potential's derivative is not defined, having a jump between z positive and z negative.

We have to account for those discontinuities in the derivative of the metric [22] (and consequently of the Christoffel symbols). To do so, we will follow [1], and expand the metric right above (+) and below (-) the plane of the disk at $z = 0$ as

$$g_{\mu\nu} = g_{\mu\nu}^0 + z g_{\mu\nu,z}^{\pm} \Big|_{z=0} + \frac{1}{2} z^2 g_{\mu\nu,zz}^{\pm} \Big|_{z=0} + \dots, \quad (15)$$

where $g_{\mu\nu}^0$ is the value of $g_{\mu\nu}$ at $z = 0$. The discontinuities of the metric are represented by the introduction of

$$b_{\mu\nu} = g_{\mu\nu,z}^+ \Big|_{z=0} - g_{\mu\nu,z}^- \Big|_{z=0}. \quad (16)$$

Moreover, we define $\Lambda^+ = \Lambda(\rho, z)$ for z positive and $\Lambda^- = \Lambda(\rho, -z)$ for z negative, and use that $\Lambda^+|_{z=0} = -\Lambda^-|_{z=0}$ and define $\Lambda^+|_{z=0} = \Lambda^-|_{z=0}$ to simplify the expressions for the non-zero elements of $b_{\mu\nu}$.

We can proceed with this reasoning in order to compute the distributed Christoffel symbols. The Christoffel symbols are given by [3]

$$\Gamma_{\mu\nu}^\alpha = \frac{1}{2}g^{\alpha\beta}(g_{\beta\nu,\mu} + g_{\mu\beta,\nu} - g_{\mu\nu,\beta}). \quad (17)$$

Introducing $[\Gamma_{\mu\nu}^\alpha] = \Gamma_{\mu\nu}^{\alpha+} - \Gamma_{\mu\nu}^{\alpha-}$ and taking the derivatives of the metric with respect to z we end up with

$$[\Gamma_{\mu\nu}^\alpha] = \frac{1}{2}(\delta_\mu^z b_\nu^\alpha + \delta_\nu^z b_\mu^\alpha - g^{\alpha z} b_{\mu\nu}). \quad (18)$$

Moving forward to the definition of the Riemann tensor [3]

$$R_{\beta\mu\nu}^\alpha = \Gamma_{\nu\beta,\mu}^\alpha - \Gamma_{\mu\beta,\nu}^\alpha + \Gamma_{\mu\lambda}^\alpha \Gamma_{\nu\beta}^\lambda - \Gamma_{\nu\lambda}^\alpha \Gamma_{\mu\beta}^\lambda, \quad (19)$$

the same reasoning applies in order to calculate the distributed Riemann tensor $[R_{\alpha\beta\mu\nu}] = R_{\alpha\beta\mu\nu}^+ - R_{\alpha\beta\mu\nu}^-$. Following [23], with the help of the distributed metric (equation 16) and distributed Christoffel symbols (equation 18), and taking in consideration that we are considering vacuum above and below the disk plane at $z = 0$, the distributed Riemann tensor becomes

$$[R_{\alpha\beta\mu\nu}] = \frac{1}{2}(\delta_\beta^z \delta_\mu^z b_{\alpha\nu} - \delta_\mu^z \delta_\alpha^z b_{\nu\beta} + \delta_\alpha^z \delta_\nu^z b_{\mu\beta} - \delta_\beta^z \delta_\nu^z b_{\mu\alpha}). \quad (20)$$

A simple calculation leads us to the distributed Ricci tensor ($R_{\alpha\beta} = R_{\alpha\mu\beta}^\mu$)

$$[R_{\beta\nu}] = \frac{1}{2}(\delta_\beta^z b_\nu^z - g^{zz} b_{\nu\beta} + \delta_\nu^z b_\beta^z - \delta_\beta^z \delta_\nu^z b_\alpha^\alpha), \quad (21)$$

and to the distributed Ricci scalar ($R = R_\alpha^\alpha = g^{\alpha\beta} R_{\alpha\beta}$)

$$[R] = \frac{1}{2} \times 2(b^{zz} - g^{zz} b_\alpha^\alpha) = b^{zz} - g^{zz} b_\alpha^\alpha. \quad (22)$$

By calculating the non-zero terms of the distributed Ricci tensor (equation 21), as well as the distributed Ricci scalar, we can calculate the components of the distributed energy-momentum $[T_\nu^\mu]$ making use of the Einstein's equations

$$[R_\nu^\mu] - \frac{1}{2}\delta_\nu^\mu [R] = 8\pi [T_\nu^\mu]. \quad (23)$$

Moreover, the components of the distributed energy-momentum are related to the general energy-momentum tensor by $T_\nu^\mu = [T_\nu^\mu] \delta(z)$, and so we have the final result

$$\epsilon = -T_t^t = e^{\Lambda-\nu}(2 - \rho\Lambda_{,\rho})\Lambda_{,z}\delta(z), \quad (24a)$$

$$p_{\varphi\varphi} = T_\varphi^\varphi = e^{\Lambda-\nu}\rho\Lambda_{,\rho}\Lambda_{,z}\delta(z), \quad (24b)$$

$$T_\rho^\rho = T_z^z = 0, \quad (24c)$$

where ϵ is the energy density and $p_{\varphi\varphi}$ the pressure density [24].

3. EQUATIONS OF MOTION

We start with the Lagrangian density

$$\mathcal{L} = \frac{1}{2}g_{\mu\nu}\dot{x}^\mu\dot{x}^\nu, \quad (25)$$

where \dot{x}^μ corresponds to a derivative with respect to the affine parameter λ . The action is given by

$$S[x^\mu] = \int_{\lambda_1}^{\lambda_2} \mathcal{L}(x^\mu, \dot{x}^\mu, \lambda)d\lambda. \quad (26)$$

By varying the action and requiring it to be stationary at the extrema, we will reach the geodesic equations [3]

$$\ddot{x}^\mu + \Gamma_{\nu\gamma}^\mu \dot{x}^\nu \dot{x}^\gamma = 0. \quad (27)$$

3.1. Killing's equation and Killing vector fields

A Killing vector field X^α is a vector field that preserves a metric g (that is, leaves the metric invariant under a certain transformation. This transformation is called an isometry [3]). The condition for the vector field X^α to be a Killing vector is thus [25]

$$\mathcal{L}_X g_{\mu\nu} = 0, \quad (28)$$

where \mathcal{L}_X is the Lie derivative, from which we easily reach Killing's equation [25]

$$\nabla_\mu X_\nu + \nabla_\nu X_\mu = 0, \quad (29)$$

where ∇_μ is the covariant derivative.

We see from equation 28 that if a metric $g_{\mu\nu}$ does not depend on a certain coordinate (for example, y), then ∂_y is a Killing vector field. Both Schwarzschild metric and Schwarzschild Black Hole + disk metric do not depend on t and φ , and so both have Killing vector fields given by ∂_t and ∂_φ , that are respectively associated with staticity and axial symmetry of the spacetimes. Moreover, they are respectively connected to the momentum components as

$$p_t = -E, \quad (30a)$$

$$p_\varphi = L. \quad (30b)$$

3.2. Equations of motion

The motion of test particles (namely photons) in the spacetime given by equation 2 must obey the geodesic equations 27. In order to compute them, we need to know the non-zero Christoffel symbols corresponding to this spacetime. The Christoffel symbols can be easily computed by plugging the metric 2 into *Mathematica* [26], alongside with the package *GRQUICK* [27]. Having the Christoffel symbols, we can proceed to the equations of motion.

For the t and φ components, the equations of motion are easier to integrate because of the constants of motion (equation 30), and thus they become first order differential equations

$$\dot{t} = g^{tt} p_t = -g^{tt} E = e^{-\phi} E, \quad (31a)$$

$$\dot{\varphi} = g^{\varphi\varphi} p_\varphi = g^{\varphi\varphi} L = \frac{e^\phi}{\rho^2} L, \quad (31b)$$

For the ρ and z equations, the geodesic equations 27 are translated into

$$\begin{aligned} \ddot{\rho} &= - \left[\Gamma_{tt}^\rho \dot{t}^2 + \Gamma_{\rho\rho}^\rho \dot{\rho}^2 + 2\Gamma_{\rho z}^\rho \dot{\rho} \dot{z} + \Gamma_{zz}^\rho \dot{z}^2 + \Gamma_{\varphi\varphi}^\rho \dot{\varphi}^2 \right] \\ &= - \left[\frac{1}{2} e^{-\nu} \phi_{,\rho} E^2 + \frac{1}{2} (\nu_{,\rho} - \phi_{,\rho}) \dot{\rho}^2 + (\nu_{,z} - \phi_{,z}) \dot{\rho} \dot{z} \right. \\ &\quad \left. + (\phi_{,\rho} - \nu_{,\rho}) \dot{z}^2 + \frac{e^{2\phi-\nu}}{2\rho^3} (-2 + \rho\phi_{,\rho}) L^2 \right], \end{aligned} \quad (32a)$$

$$\begin{aligned} \ddot{z} &= - \left[\Gamma_{tt}^z \dot{t}^2 + \Gamma_{\rho\rho}^z \dot{\rho}^2 + 2\Gamma_{\rho z}^z \dot{\rho} \dot{z} + \Gamma_{zz}^z \dot{z}^2 + \Gamma_{\varphi\varphi}^z \dot{\varphi}^2 \right] \\ &= - \left[\frac{1}{2} e^{-\nu} \phi_{,z} E^2 + \frac{1}{2} (\phi_{,z} - \nu_{,z}) \dot{\rho}^2 + (\nu_{,\rho} - \phi_{,\rho}) \dot{\rho} \dot{z} \right. \\ &\quad \left. + \frac{1}{2} (\nu_{,z} - \phi_{,z}) \dot{z}^2 + \frac{e^{2\phi-\nu}}{2\rho^2} \phi_{,z} L^2 \right], \end{aligned} \quad (32b)$$

and the first order differential equations are given by

$$\frac{d\rho}{d\lambda} = v_\rho, \quad (33a)$$

$$\frac{dz}{d\lambda} = v_z, \quad (33b)$$

where v_ρ and v_z are velocities in the ρ and z directions, respectively.

4. SHADOW AND LENSING OF A BLACK HOLE

The Black Hole shadow can be associated with the Black Holes light absorption cross-section at high frequencies, and its edge is associated with a set of unstable

light rings [28]. The shape of the shadow is uniquely determined [29] by the mass, spin and inclination of the Black Hole, and it can be accounted as an observable that allows us to test the true nature of the spacetime around a Black Hole. We can check that Numerically, the process is as follows: imagine that we have a spherical background setup which we call numerical infinity (as in (a) from figure 2), and that inside that sphere are both an observer and a Black Hole. If we were dealing, for example, with flat spacetime, we would have a correspondence 1-on-1 between the observer \mathcal{O} (where the light is numerically emitted) and the background setup \mathcal{N} where the light arrives, that is, a map $\mathcal{I} : \mathcal{O} \rightarrow \mathcal{N}$ ((b) from figure 2). However, if together with the observer there was a Black Hole, some of the light rays from \mathcal{O} would not reach (or would not be mapped into) \mathcal{N} . Numerically, this set of points is what we name the Black Hole shadow, with an example shown in (c) from figure 2.

4.1. Backwards Ray-tracing

Propagating all the photons from a certain region of the spacetime would be extremely costly, and a significant number of them would not even reach the observer. Instead, we propagate the photons backwards in time from the point where the observer is, until they reach either the Black Hole or the sphere that we consider as our numerical infinity. This backwards propagation process is a much more effective process.

Our local observer basis, based on the tetrad formalism [31], will be constructed of 4 basis vectors (4-dimensional spacetime) $\hat{e}_{(a)}^\mu$ that must obey

$$\hat{e}_\mu^{(a)} \left(\hat{e}_{(b)}^\mu \right) = \delta_{(b)}^{(a)}, \quad (34a)$$

$$\hat{e}_\mu^{(a)} \left(\hat{e}_{(a)}^\nu \right) = \delta_\nu^\mu, \quad (34b)$$

where the latin letters refer to the tetrad indices, and greek letters refer to the tensor indices. Focusing on the system Black Hole + disk, the observer basis $\{\hat{e}_{(t)}, \hat{e}_{(\rho)}, \hat{e}_{(z)}, \hat{e}_{(\varphi)}\}$ can be expanded in the coordinate basis $\{\partial_t, \partial_\rho, \partial_z, \partial_\varphi\}$, and a possible choice is ([32, 33]), where $(\zeta, \gamma, A^\rho, A^z, A^\varphi)$ are real coefficients. This particular choice is ([33]) "connected to a reference frame with zero axial angular momentum in relation to spatial infinity, and hence it is sometimes called the ZAMO reference frame". The observer basis has a Minkowski normalization

$$\hat{e}_{(a)} \cdot \hat{e}_{(a)} = \begin{cases} 1, & \alpha = \rho, z, \varphi \\ -1 & \alpha = t \end{cases}, \quad (35)$$

and must fulfill the requirement

$$\hat{e}_{(t)} \cdot \hat{e}_{(\varphi)} = 0. \quad (36)$$

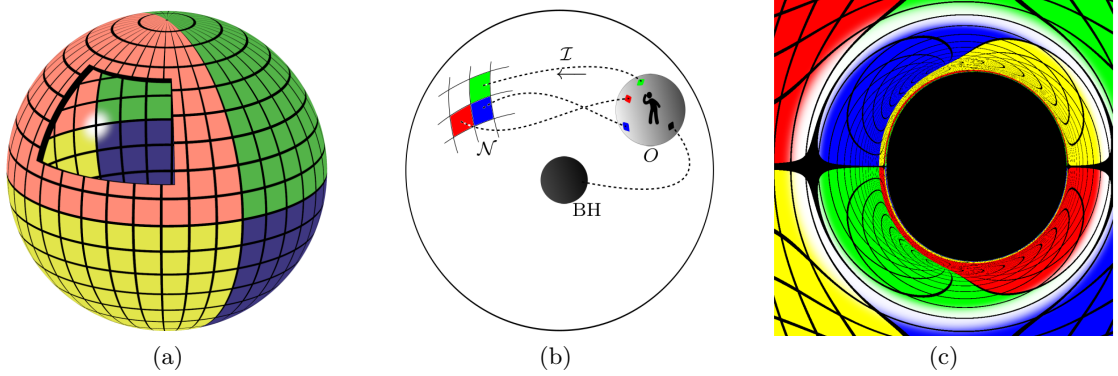


FIG. 2: Setup for imaging a Black Hole shadow. a) Artificial background grid "painted on" a sphere on infinity (adapted from [30]) ; b) Schematics of the mapping setup (adapted from [7]) ; c) Example of observational image for a Kerr BH with $a/M \approx 0.82$ (adapted from [7]).

Using equation 35 it is easy to reach that

$$A^z = \frac{1}{\sqrt{g_{zz}}} \quad A^\rho = \frac{1}{\sqrt{g_{\rho\rho}}}, \quad A^\varphi = \frac{1}{\sqrt{g_{\varphi\varphi}}}. \quad (37)$$

With the help of equation 36, and because A^φ and $g_{\varphi\varphi}$ are different from zero, we have that

$$\gamma = 0, \quad \zeta = \sqrt{-\frac{1}{g_{tt}}}. \quad (38)$$

We can also compute the local measured momentum components and their projection in 4-momentum [32]. For time component, we have $p^{(t)} = -(\hat{e}_{(t)}^\mu p_\mu) = -(\zeta p_t + \gamma p_\varphi)$ and for the spatial components $p^{(i)} = (\hat{e}_{(i)}^\mu p_\mu)$. In this spacetime, as mentioned before in section 3.3.1), we have two constants of motion that are identified with the energy \mathbf{E} : $E = -p_t$; and with the angular momentum \mathbf{L} : $p_\varphi = L$, and so we have that

$$\begin{aligned} p^{(t)} &= E\zeta & p^{(z)} &= \frac{1}{\sqrt{g_{zz}}}p_z \\ p^{(\varphi)} &= \frac{1}{\sqrt{g_{\varphi\varphi}}}L & p^{(\rho)} &= \frac{1}{\sqrt{g_{\rho\rho}}}p_\rho \end{aligned} \quad (39)$$

The components of the photon's linear momentum \vec{P} in the observer's basis $\{\hat{e}_{(\rho)}, \hat{e}_{(z)}, \hat{e}_{(\varphi)}\}$ are $p^{(\rho)}$, $p^{(z)}$ and $p^{(\varphi)}$, and so its square modulus is given by

$$|\vec{P}|^2 = \left(p^{(\rho)}\right)^2 + \left(p^{(z)}\right)^2 + \left(p^{(\varphi)}\right)^2. \quad (40)$$

Following [33], we can parametrize the components of \vec{P} by two angles, α and β , as

$$\begin{aligned} p^{(\rho)} &= |\vec{P}| \cos \beta \sin \alpha, \\ p^{(z)} &= |\vec{P}| \sin \alpha, \\ p^{(\varphi)} &= |\vec{P}| \sin \beta \cos \alpha. \end{aligned} \quad (41)$$

Since we are dealing with photons (zero mass particles), we have that $P_\mu P^\mu = 0$ and so $p^{(t)} = |\vec{P}|$. As a consequence of equation 39, we can finally write the initial conditions for the photons' momenta parametrized by α and β

$$\begin{aligned} -p_t &= E = \frac{|\vec{P}|}{\zeta}, \\ p_\rho &= |\vec{P}| \sqrt{g_{\rho\rho}} \cos \beta \cos \alpha, \\ p_z &= |\vec{P}| \sqrt{g_{zz}} \sin \alpha, \\ p_\varphi &= L = |\vec{P}| \sqrt{g_{\varphi\varphi}} \sin \beta \cos \alpha. \end{aligned} \quad (42)$$

A comment must be made ([33]): the value of $|\vec{P}|$ is redundant because it only establishes the photons' frequency, and does not influence their trajectories. Because of that, we can set it to 1.

4.2. Grid setup

The definition of angles (α, β) is also crucial to reach our main goal, that is, to have a numerical image of the shadow (and lensing) of a system with a Black Hole. We can identify them as the field of view of the observer. The bigger the angles are, the bigger the field of view of the observer becomes. Prior to propagating the photons in any other spacetime, we have to set our background sphere and its corresponding image in Minkowski spacetime, in order to associate a pixel of the image to each pair (α, β) . That is, we discretize the image in a matrix, where each point of the matrix corresponds to a certain pair of (α, β) (and consequently, to a certain initial 4-momentum of a photon).

With this in mind, we can consider a spacetime with a Black Hole. Doing the same process as before, a photon with initial conditions described by (α, β) is backwards ray-traced until it reaches either

- the Black Hole - a black pixel is assigned to that photon (and to the corresponding entry in the matrix);
- the background sphere - depending on the final conditions of the photon, a comparison with the flat spacetime final conditions is performed, and the corresponding color of the background is assigned to that photon.

4.3. The numerical code

The numerical code that allows us to integrate numerically the equations of motion in a given spacetime (either the Schwarzschild Black Hole case or Schwarzschild + disk case) consists of a Runge-Kutta-Fehlberg method with adaptive step, written in Python3 [34]. The Runge-Kutta-Fehlberg method [35] is a method of order $O(h^4)$, with an error estimator of order $O(h^5)$, that allows us to have an adaptive step that is found automatically.

Moreover, although in the Schwarzschild Black Hole case we know both the metric potentials (equation 7), in the Black Hole + disk case we have only an analytical formula for the $\Psi + \Lambda$ potential (equation 12). To calculate the potential $\nu[\Psi + \Lambda]$, we have to evaluate numerically the integral in equation 4 at each point of the trajectory. However, this process is very costly computationally. The solution found to overcome this problem was to set an highly discretized matrix with the values of the potential $\nu[\Psi + \Lambda]$, prior to the evolution of the equations of motion. Having set the matrix for the ν potential, we can compute the value of ν at any point of the spacetime by applying the bilinear interpolation method [36].

5. RESULTS

The results presented in this section contain both the lensing and the imaging of the Shadow of the system Black Hole + disk. Each image has been generated by a 1000x1000 matrix, that is originated by discretizing the angles α and β in two arrays of 1000 values each (both angles are set in the interval $[\tan^{-1}(10/15); \tan^{-1}(10/15)]$). The Runge-Kutta-Fehlberg method used had a maximum step of $h_{\max} = 0.02$, a minimum step of $h_{\min} = 10^{-7}$, and a tolerance $\text{tol} = 10^{-4}$.

Prior to the numerical study of the system Black Hole + disk, in order to test the code, we did the backwards ray-tracing of a spacetime where the mass of the disk was set to zero, that is, the spacetime of a Schwarzschild Black Hole, that is shown in figure 3. The lensing of such a spacetime had already been studied before by Bohn *et al.*, and the image we obtained is similar to the one in [30].

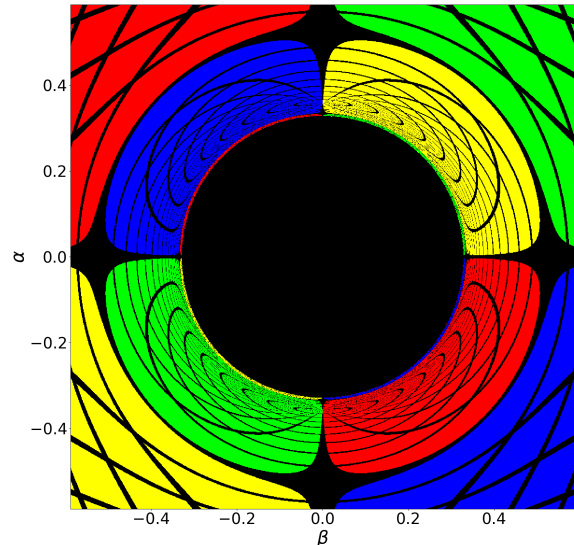


FIG. 3: Lensing of Schwarzschild Black Hole with mass $M = 1$. The observer is at initial position $r_0 = 15$, in the equatorial plane ($\theta_0 = \pi/2$). The background sphere is at $r = 30$.

5.1. Constraints on the numerically generated solutions

As mentioned in section 2.2.2, some particles that compose the Morgan-Morgan disk have tachyonic speeds. In Lemos-Letelier disk, the same happens for certain values of $(M_{BH}, M_{\text{disk}}, a)$, signaling that these solutions are unphysical ones, and thus reducing the number of possible numerical integrations to perform.

But first, we must take in consideration that we just need to constrain 2 parameters: we are setting the total mass of the system Black Hole + disk to 1 in order to have comparable solutions in our simulations. Because of that, we are constraining only (M_{BH}, a) , being the mass of the disk obtained immediately by $M_{\text{disk}} = 1 - M_{BH}$.

The velocity of the particles is given by [1, 37]

$$V^2 = \frac{p_{\varphi\varphi}}{\epsilon}, \quad (43)$$

where $p_{\varphi\varphi}$ and ϵ are defined in equation 24.

We can find numerically the values of V^2 , and consequently, the physically allowed ($0 \leq V^2 \leq 1$) and forbidden ($V^2 < 0$ or $V^2 > 1$) regions. These regions are shown in figure 4, where the physically allowed regions are represented by the white color. All the other three colors (blue, grey and red) represent the physically forbidden regions: the blue color represents the region where there are values of $V^2 > 1$; the red color represents the region where there are values of $V^2 < 0$; finally, the grey

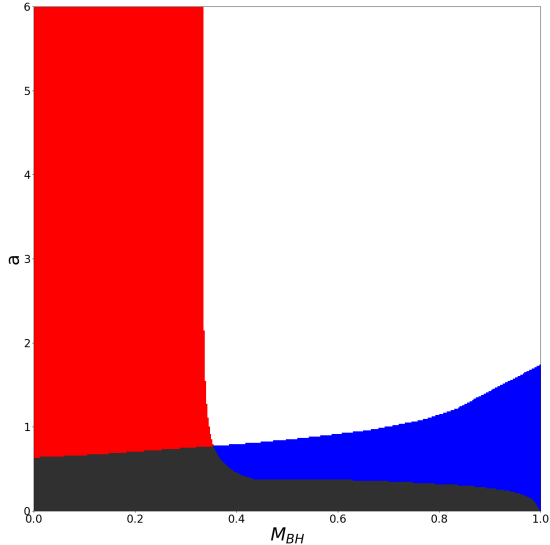


FIG. 4: Physically allowed (white) and forbidden (blue, grey and red) regions for a given choice of (M_{BH}, a) .

color represents the region where there are both values of $V^2 > 1$ and $V^2 < 0$.

5.2. Shadow of Black Hole + disk

The initial conditions of the observer are given by a radial coordinate ρ_{obs} that is given by the perimetral radius (as defined in [33]), and a z coordinate $z_{\text{obs}} = 0$. Moreover, in this case, the accretion disk illuminates the spacetime by emitting light.

Regarding the stopping conditions for the imaging of the shadow, they are

- If at a point of the trajectory of a photon corresponds a metric potential $\phi(\rho, z) < -3.0$, the photon reached the Black Hole region and a black pixel will be assigned to that photon;
- If a photon has a radial coordinate $\rho > a$ and the z -component of its trajectory changes from positive (negative) z to negative (positive) z , the photon reached the disk. A white pixel is assigned to that photon;
- If a photon has a perimetral radius $\tilde{r} > 30$, the photon reached the background and a grey pixel is assigned to that photon. This condition makes use of the properties of the perimetral radius to measure distances, where the perimetral radius is given by $\sqrt{g_{\varphi\varphi}}(\rho = \sqrt{\rho^2 + z^2}, z = 0, M_{BH}, a)$, and also

that for ρ, z big, the background can be approximated by a sphere of radius $\sqrt{\rho^2 + z^2}$.

The results shown in figure 5 correspond to set the inner edge of the disk to a constant value, $a = 3.0$. We see that for smaller masses of the Black Hole (and consequently for large masses of the disk), due to the disk's weight, the photons are attracted to the disk and end up falling there. Although the disk is thin, we see an optical enlargement of the disk in the first images of figure 5, that becomes smaller as the mass of the Black Hole increases. Moreover, for smaller masses of the Black Hole, the shape of the shadow is similar to a prolate spheroid. As we increase the mass of the Black Hole, the shadow shape becomes more circular, and as expected its size also increases. Besides that, for larger masses of the Black Hole, the behavior of the system corresponds to what is expected: the disk is in fact represented as thin, and if we took the disk part of the bottom right image with $M_{BH} = 0.9$, it would be tremendously similar to the Schwarzschild solution's shadow (figure 3).

5.3. Lensing of Black Hole + disk

The initial conditions of the observer are analogous to the former section, but contrary to the shadow case, the spacetime is now illuminated by the background sphere, being the disk transparent (the photons do not stop on the disk, just pass through it).

Regarding the stopping conditions, we just need two of the conditions of the imaging of the shadow: the condition for Black Hole (corresponding to a Black pixel) and the condition for the background, that depending on the final position of the photon ($\rho_{\text{final}}, z_{\text{final}}, \varphi_{\text{final}}$), it will correspond to one of the colors of the background (red, green, blue, yellow) or the grid (black).

However, one must be careful with the transmission of the photons in the disk, due to the disk potential's shape, and the fact that the potential has a jump in its derivatives in the z -direction. To deal with the problem, we can think of a classical mechanics analogy: a ball that is rolling through an horizontal plane (path 1) and finds an inclined plane (path 2), being the intersection of the two paths cuspy. Although the acceleration has a discontinuity at the intersection of the paths, the velocity immediately before (at the end of path 1) and the velocity immediately after the intersection (beginning of path 2) are the same, that is, the velocity is continuous. In our case, due to the similarities with the classical mechanics analogy, the conclusions are the same: the velocity of the photons through the disk does not have, for example, a jump: it is continuous.

Again, the inner edge of the disk is set to a constant value $a = 3.0$, and the results are shown in figure 6. From the images corresponding to $M_{\text{disk}} = 0.6$, $M_{\text{disk}} = 0.5$, $M_{\text{disk}} = 0.4$ (which correspond to $M_{\text{disk}} = 1.5M_{BH}$, $M_{\text{disk}} = M_{BH}$, $M_{\text{disk}} = \frac{2}{3}M_{BH}$, respectively), we see

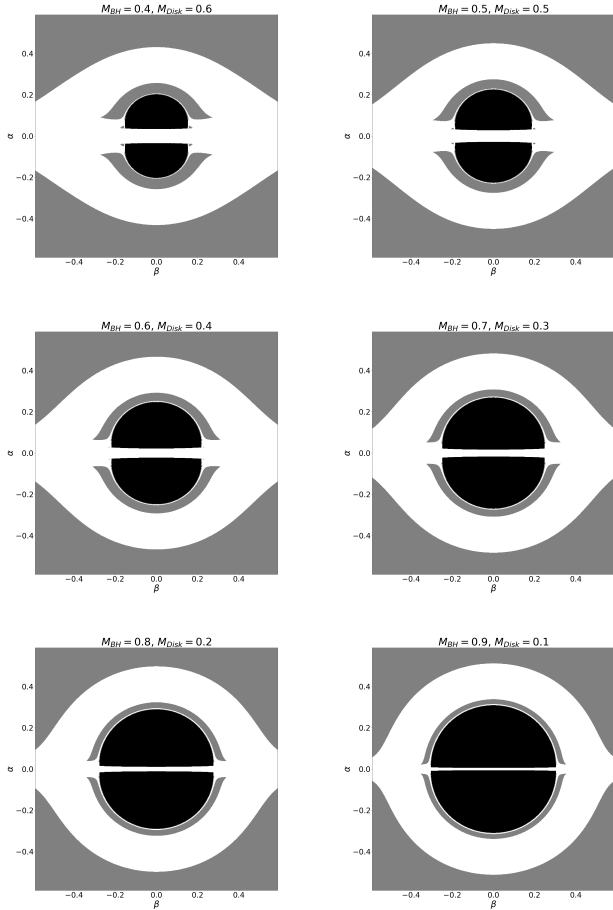


FIG. 5: Shadow of the Black Hole + disk with fixed $a = 3.0$: a) $M_{BH} = 0.4$ and $M_{disk} = 0.6$, b) $M_{BH} = 0.5$ and $M_{disk} = 0.5$, c) $M_{BH} = 0.6$ and $M_{disk} = 0.4$, d) $M_{BH} = 0.7$ and $M_{disk} = 0.3$, e) $M_{BH} = 0.8$ and $M_{disk} = 0.2$, f) $M_{BH} = 0.9$ and $M_{disk} = 0.1$.

how deformed the spacetime becomes when comparing with figure 3, that represents the lensing from the Schwarzschild Black Hole. Besides that, as seen before, the shadow's shape has some resemblance to a prolate spheroid. As we increase the mass of the Black Hole (figures corresponding to $M_{BH} = 0.7$, $M_{BH} = 0.8$, $M_{BH} = 0.9$), the shape of the shadow becomes more circular, and the lensing of the background more similar to figure 3.

6. CONCLUSION

In this thesis, an objective was clearly established: to study the behavior of a spacetime where a thin massive disk of matter surrounding a Schwarzschild Black Hole is present, keeping in mind the astrophysical relevance of the solution. To do so, we studied the system in Weyl coordinates, with a special focus in the disk plane, due

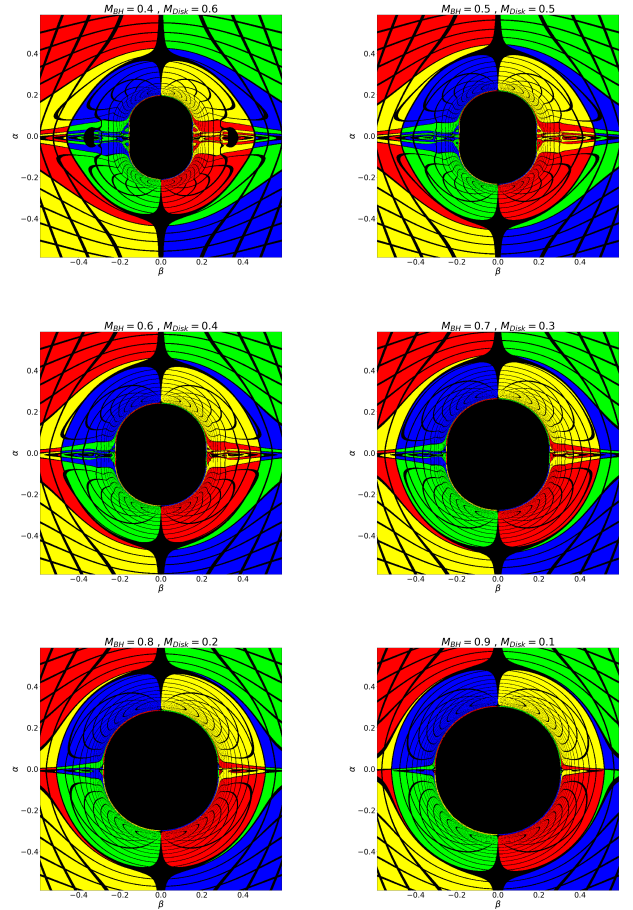


FIG. 6: Lensing of the Black Hole + disk with fixed $a = 3.0$: a) $M_{BH} = 0.4$ and $M_{disk} = 0.6$, b) $M_{BH} = 0.5$ and $M_{disk} = 0.5$, c) $M_{BH} = 0.6$ and $M_{disk} = 0.4$, d) $M_{BH} = 0.7$ and $M_{disk} = 0.3$, e) $M_{BH} = 0.8$ and $M_{disk} = 0.2$, f) $M_{BH} = 0.9$ and $M_{disk} = 0.1$.

to the jump on the derivatives of the disk. Moreover, a backwards ray-tracing technique was developed and implemented in the code, alongside with an adaptive step-size Runge-Kutta-Fehlberg algorithm.

The path described above culminates in the results of section 5, where we see clearly how does a thin massive disk around a central Black Hole deforms the spacetime when compared with a spacetime that only has a Schwarzschild Black Hole in it. Indeed, the differences are notorious, both in the pattern of the lensing of a background image, as well as in the shape of the shadow of the Black Hole.

Acknowledgments

I want to thank to both my supervisors Prof. Carlos Herdeiro and Dr. Pedro Cunha for all the discussions, guidance and patience throughout this thesis.

-
- [1] J. P. S. Lemos and P. S. Letelier, *Phys. Rev. D* **49**, 5135 (1994).
- [2] T. Morgan and L. Morgan, *Phys. Rev.* **183**, 1097 (1969).
- [3] R. D’Inverno, *Introducing Einstein’s Relativity* (Clarendon Press, 1992).
- [4] G. Birkhoff and R. Langer, *Relativity and Modern Physics* (Harvard University Press, 1923).
- [5] M. Heusler, *Black Hole Uniqueness Theorems*, Cambridge Lecture Notes in Physics (Cambridge University Press, 1996).
- [6] P. T. Chrusciel, J. L. Costa, and M. Heusler, *Living Rev. Rel.* **15** (2012), 1205.6112.
- [7] P. V. P. Cunha and C. A. R. Herdeiro, *Gen. Rel. Grav.* **50**, 42 (2018), 1801.00860.
- [8] Event Horizon Telescope Collaboration, K. Akiyama, et al. (Event Horizon Telescope), *Astrophys. J.* **875**, L2 (2019), 1906.11239.
- [9] Event Horizon Telescope Collaboration, K. Akiyama, et al., *Astrophys. J.* **875**, L1 (2019), 1906.11238.
- [10] Event Horizon Telescope Collaboration, K. Akiyama, et al., *Astrophysics. J.* **875**, L3 (2019), 1906.11240.
- [11] Event Horizon Telescope Collaboration, K. Akiyama, et al. (Event Horizon Telescope), *Astrophys. J.* **875**, L4 (2019), 1906.11241.
- [12] Event Horizon Telescope Collaboration, K. Akiyama, et al. (Event Horizon Telescope), *Astrophys. J.* **875**, L5 (2019), 1906.11242.
- [13] Event Horizon Telescope Collaboration, K. Akiyama, et al., *Astrophys. J.* **875**, L6 (2019), 1906.11243.
- [14] D. Psaltis, arXiv e-prints arXiv:1806.09740 (2018), 1806.09740.
- [15] P. V. P. Cunha, C. A. R. Herdeiro, E. Radu, and H. F. Rúnarsson, *Phys. Rev. Lett.* **115**, 211102 (2015).
- [16] O. Semerak and P. Sukova, *Mon. Not. Roy. Astron. Soc.* **404**, 545 (2010), 1211.4106.
- [17] J. B. Griffiths and J. Podolsky, *Exact Space-Times in Einstein’s General Relativity*, Cambridge Monographs on Mathematical Physics (Cambridge University Press, Cambridge, 2009), ISBN 9781139481168.
- [18] D. Lynden-Bell and S. Pineault, *Monthly Notices of the Royal Astronomical Society* **185**, 679 (1978), ISSN 0035-8711.
- [19] W. Research, *Kelvin transformation*, <http://mathworld.wolfram.com/KelvinTransformation.html>, accessed 07 August 2019.
- [20] P. S. Letelier and S. R. Oliveira, *Journal of Mathematical Physics* **28**, 165 (1987).
- [21] H. Bateman, *Partial Differential Equations of Mathematical Physics* (Cambridge U.P, 1932).
- [22] A. H. Taub, *Journal of Mathematical Physics* **21**, 1423 (1980).
- [23] A. Huber, arXiv e-prints arXiv:1908.08735 (2019), 1908.08735.
- [24] D. Lynden-Bell and S. Pineault, *Monthly Notices of the Royal Astronomical Society* **185**, 695 (1978), ISSN 0035-8711.
- [25] R. Wald, *General Relativity* (University of Chicago Press, 2010), ISBN 9780226870373.
- [26] W. R. Inc., *Mathematica, Version 11.3*, champaign, IL, 2018.
- [27] J. Varela, *GRQUICK*, <http://library.wolfram.com/infocenter/MathSource/8329/>, accessed 16 August 2019.
- [28] P. V. P. Cunha, C. A. R. Herdeiro, and M. J. Rodriguez, *Phys. Rev. D* **97**, 084020 (2018), 1802.02675.
- [29] T. Johannsen, *Astrophys. J.* **777**, 170 (2013), 1501.02814.
- [30] A. Bohn, W. Thrope, F. Hbert, K. Henriksson, D. Bunandar, M. A. Scheel, and N. W. Taylor, *Class. Quant. Grav.* **32** (2015), 1410.7775.
- [31] S. Chandrasekhar, *The Mathematical Theory of Black Holes*, International series of monographs on physics (Oxford University Press, 1992).
- [32] J. M. Bardeen, in *Proceedings, Ecole d’Et de Physique Thorique: Les Astres Occlus: Les Houches, France, August, 1972* (1973), pp. 215–240.
- [33] P. V. P. Cunha, C. A. R. Herdeiro, E. Radu, and H. F. Runarsson, *Int. J. Mod. Phys. D* **25** (2016), 1605.08293.
- [34] Python, *Python3*, <http://www.python.org/>, accessed 14 August 2019.
- [35] A. Iserles, *A First Course in the Numerical Analysis of Differential Equations*, Cambridge Texts in Applied Mathematics (Cambridge University Press, 2008), 2nd ed.
- [36] W. Press, *Numerical Recipes in C: The Art of Scientific Computing*, liv. 4 (Cambridge University Press, 1992), ISBN 9780521437202.
- [37] J. P. S. Lemos, *Classical and Quantum Gravity* **6**, 1219 (1989).